ADVANCED OPTICAL MATERIALS
www.advopticalmat.de

Check for updates

2D $MoSe_2$ Geometrically Asymmetric Schottky Photodiodes

Hamidreza Ghanbari, Amin Abnavi, Ribwar Ahmadi, Mohammad Reza Mohammadzadeh, Mirette Fawzy, Amirhossein Hasani, and Michael M. Adachi**

Optoelectronic devices based on geometrically asymmetric architecture have recently attracted attention due to their high performance as photodetectors and simple fabrication process. Herein, a p-type 2D $MoSe_2$ photodetector based on geometrically asymmetric contacts is reported for the first time. The device exhibits a high current rectification ratio of ≈10^4 and a large self-powered photovoltage responsivity of ≈4.38×10^7 V W^{-1}, as well as a maximum photocurrent responsivity of ≈430 mA W^{-1} along with a response time of ≈2.3 ms under 470 nm wavelength at 3 V bias voltage. The photocurrent responsivity is further enhanced to an ultrahigh responsivity of ≈1615 mA W^{-1} by applying a gate bias voltage due to the electrostatic modulation of carrier concentration in the $MoSe_2$ channel. The simple fabrication process of the geometrically asymmetric $MoSe_2$ diodes along with their high photodetection and diode rectifying performance make them excellent candidates for electronic and optoelectronic applications.

1. Introduction

Self-powered photodetectors (SPPDs) are a type of optoelectronic device that can detect photons and generate an electrical signal without the need for an external power source.[1,2] Such photodetectors are particularly useful in scenarios where it is challenging or impractical to provide a continuous power source to the photodetector such as applications in remote sensing,[3] wearable electronics,[4] Internet of Things (IoT),[5] and other low-power and energy-efficient systems.[6] There are a few different mechanisms through which self-powered photodetectors can operate including I) photovoltaic effect,[7] II) triboelectric effect,[8] III) piezoelectric effect,[9] IV) pyroelectric effect.[10] 2D transition metal dichalcogenide (TMD) materials have gained significant attention in the field of optoelectronics due to their high absorption coefficient,[11] fast carrier dynamics,[12] layer dependent properties,[13] and mechanical flexibility.[14]

SPPDs based on 2D TMDs often take advantage of the photovoltaic effect to generate electrical signals in response to incident light. In this mechanism, the photogenerated electron/hole carriers can be separated by an electric field within the material, which is created by using p-n or Schottky junctions.[15] Schottky junction-based SPPDs offer some favorable characteristics such as simplicity in fabrication, requiring no semiconductor doping process, and ultrafast response times.[16] One way to fabricate Schottky junction-based SPPDs is by using a semiconductor between two metal electrodes with different work functions. For instance, Han et al., have reported a Pd- Bi_2O_2Se-In photodetector structure with a self-powered responsivity of 1.2 A W^{-1} under 500 nm light irradiation.[17] In another report, a self-powered photodetector with a high photoresponsivity of 7.55 A W^{-1} has been developed based on an asymmetric electrode structure of Au-WSe_2-Graphene.[18] Recently, it has been demonstrated that a self-powered photodetector can be realized by using geometrically asymmetric metal/semiconductor interfaces while using the same metal electrodes at drain and source, which greatly simplifies the fabrication process of the photodetectors. High-performance SPPDs based on asymmetric geometry Ni-WSe_2-Ni and Ti-In_2S_3-Ti structures with high responsivities of 2.31 A W^{-1} and 740 mA W^{-1} are reported, respectively.[19,20] Gao et al., and Chen et al., have also reported high-performance WS_2 and InSe metal-semiconductor-metal (MSM) SPPDs with asymmetric Schottky barrier heights.[21,22] We have also previously developed a geometrically asymmetric MoS_2 SPPD with a responsivity of ≈490 mA W^{-1} and a fast response time of ≈0.8 ms under

H. Ghanbari, A. Abnavi, R. Ahmadi, M. R. Mohammadzadeh, M. M. Adachi
School of Engineering Science
Simon Fraser University
8888 University Drive, Burnaby, British Columbia V5A 1S6, Canada
E-mail: Amin_Abnavi@sfu.ca; mmadachi@sfu.ca

M. Fawzy
Department of Physics
Simon Fraser University
8888 University Drive, Burnaby, British Columbia V5A 1S6, Canada

A. Hasani
Department of Physics
Montana State University
Bozeman, MT 59717, USA

A. Hasani
MonArk NSF Quantum Foundry
Montana State University
Bozeman, MT 59717, USA

The ORCID identification number(s) for the author(s) of this article can be found under https://doi.org/10.1002/adom.202401682

© 2024 The Author(s). Advanced Optical Materials published by Wiley-VCH GmbH. This is an open access article under the terms of the Creative Commons Attribution License, which permits use, distribution and reproduction in any medium, provided the original work is properly cited.

DOI: 10.1002/adom.202401682

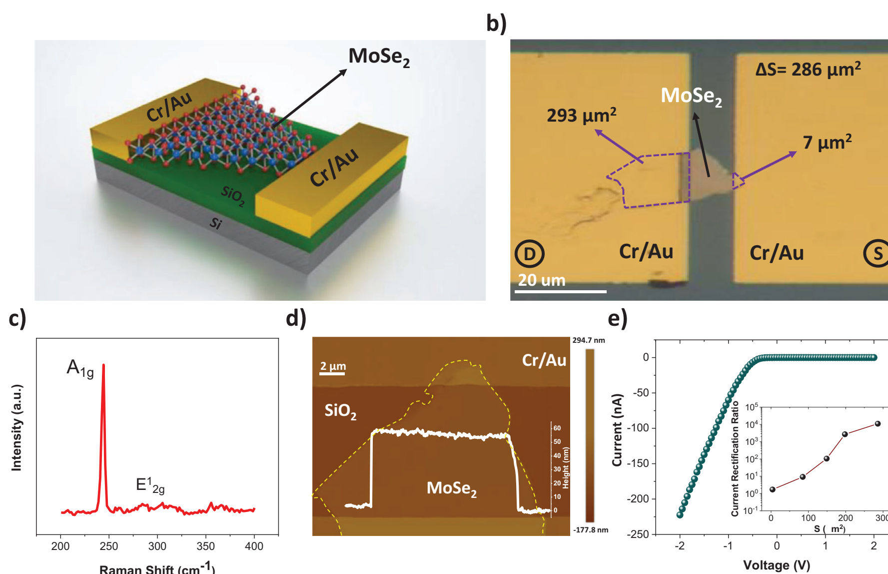

Figure 1. Device schematic, structural, and electrical characterization of the GA-$MoSe_2$ device. a) Schematic illustration of the GA-$MoSe_2$ device. b) Optical microscopy image of the GA-$MoSe_2$. Dashed lines represent two Cr-$MoSe_2$ contact areas. c) Raman Spectroscopy of the multilayer $MoSe_2$ flake, indicating the 2H phase. d) AFM image of the GA-$MoSe_2$ device, exhibiting the thickness of $MoSe_2$ flake is ≈55 nm and it is uniform. e) The linear *I–V* characteristics of the GA-$MoSe_2$ device under dark conditions show a current rectification ratio of $\approx 10^4$. The inset of panel of e depicts the current rectification ratio for different GA-$MoSe_2$ devices with different ΔS values.

450 nm.[23] The performance of such devices was found to be dependent on the Schottky barrier height difference at the drain and source sides, which is dependent on the MoS_2 thickness and MoS_2/metal interface contact areas.[23] However, the working mechanism of asymmetric geometry photodiodes remains a topic of debate, and reports of asymmetric geometry devices based on p-type 2D semiconducting materials are limited.

Herein, a photovoltaic device based on geometrically asymmetric p-type 2D molybdenum diselenide ($MoSe_2$) (GA-$MoSe_2$) is reported for the first time. The GA-$MoSe_2$ device (Au-Cr-$MoSe_2$-Cr-Au), exhibits a high current rectification ratio of $\approx 10^4$, which highly depends on the contact area asymmetry between drain and source. The high rectification ratio of the GA-$MoSe_2$ diode facilitates its application for electronic half-wave rectifiers at high frequencies. Additionally, the rectifying behavior of this device results in a large self-powered photovoltage responsivity of $\approx 4.38 \times 10^7$ V W^{-1} and a maximum photocurrent responsivity of ≈430 mA W^{-1} under 470 nm wavelength at 3 V bias voltage. The gate modulation of the carrier concentrations in the $MoSe_2$ channel further enhanced the photocurrent responsivity to ≈1615 mA W^{-1} at a gate bias of −15 V. Through photocurrent mapping on the $MoSe_2$ devices with symmetric and asymmetric architectures, the mechanism behind the photovoltaic effect is attributed to the asymmetric Schottky barriers at the $MoSe_2$/Cr interfaces. The simple fabrication process, high photovoltage/photocurrent responsivities, fast response time, and excellent flexibility of the GA-$MoSe_2$ diodes make them great candidates for flexible electronics and optoelectronic devices.

2. Results and Discussion

Geometrically asymmetric devices were fabricated using mechanically exfoliated geometrically asymmetric $MoSe_2$ crystals (GA-$MoSe_2$). The fabrication process of the devices is shown in Figure S1 (Supporting Information). **Figure 1a** shows the schematic illustration of the GA-$MoSe_2$ device; the $MoSe_2$ crystal has uneven overlapped areas with Cr metal contacts at both sides. Figure 1b shows the optical image of the GA-$MoSe_2$ device with asymmetric $MoSe_2$/Cr contact areas of 7 and 293 μm^2, resulting in a contact area difference (ΔS) of 286 μm^2. The Raman Spectroscopy of the $MoSe_2$ flakes reveals two peaks including a sharp peak for out-of-plane mode (A_{1g}) at 244 cm^{-1} and a small peak for in-plane vibration mode ($E^1{}_{2g}$) at 285 cm^{-1}, confirming the 2H semiconducting phase of $MoSe_2$[24] (Figure 1c). AFM characterization was also performed on the device, showing a uniform thickness of ≈55 nm (Figure 1d). Figure 1e illustrates the linear *I–V* curve of the GA-$MoSe_2$ device, revealing a current rectification ratio of $\approx 10^4$ under dark conditions. The Inset of Figure 1e shows that the current rectification ratio increases from ≈1.7 to $\approx 10^4$ with increasing the $MoSe_2$/Cr contact area difference at two sides from 4 to 286 μm^2, respectively. The corresponding *I–V* characteristics and optical images of these devices are depicted in Figure S2 (Supporting Information). The rectifying behavior in the devices with asymmetric architecture is attributed to the asymmetric Schottky barriers at $MoSe_2$/Cr interfaces.[23] The kelvin probe force microscopy (KPFM) characterization shows the difference in surface potential at both small and large $MoSe_2$/Cr interfaces (Figure S3, Supporting Information), which confirms the formation of a larger Schottky barrier at the larger Cr-$MoSe_2$ interface. The relative Schottky barrier heights for both symmetric and asymmetric $MoSe_2$ devices were also calculated based on the *I–V* curve fittings[25] (Section I and Figure S4, Supporting Information).

Figure 2a shows the log-scale *I–V* characteristics of the GA-$MoSe_2$ device with a high current rectification ratio of $\approx 10^4$ at dark conditions. The ideality factor of the GA-$MoSe_2$ is

© 2024 The Author(s). Advanced Optical Materials published by Wiley-VCH GmbH

21951071, 0, Downloaded from https://onlinelibrary.wiley.com/doi/10.1002/adom.202401682 by Simon Fraser University, Wiley Online Library on [20/09/2024]. See the Terms and Conditions (https://onlinelibrary.wiley.com/terms-and-conditions) on Wiley Online Library for rules of use; OA articles are governed by the applicable Creative Commons License

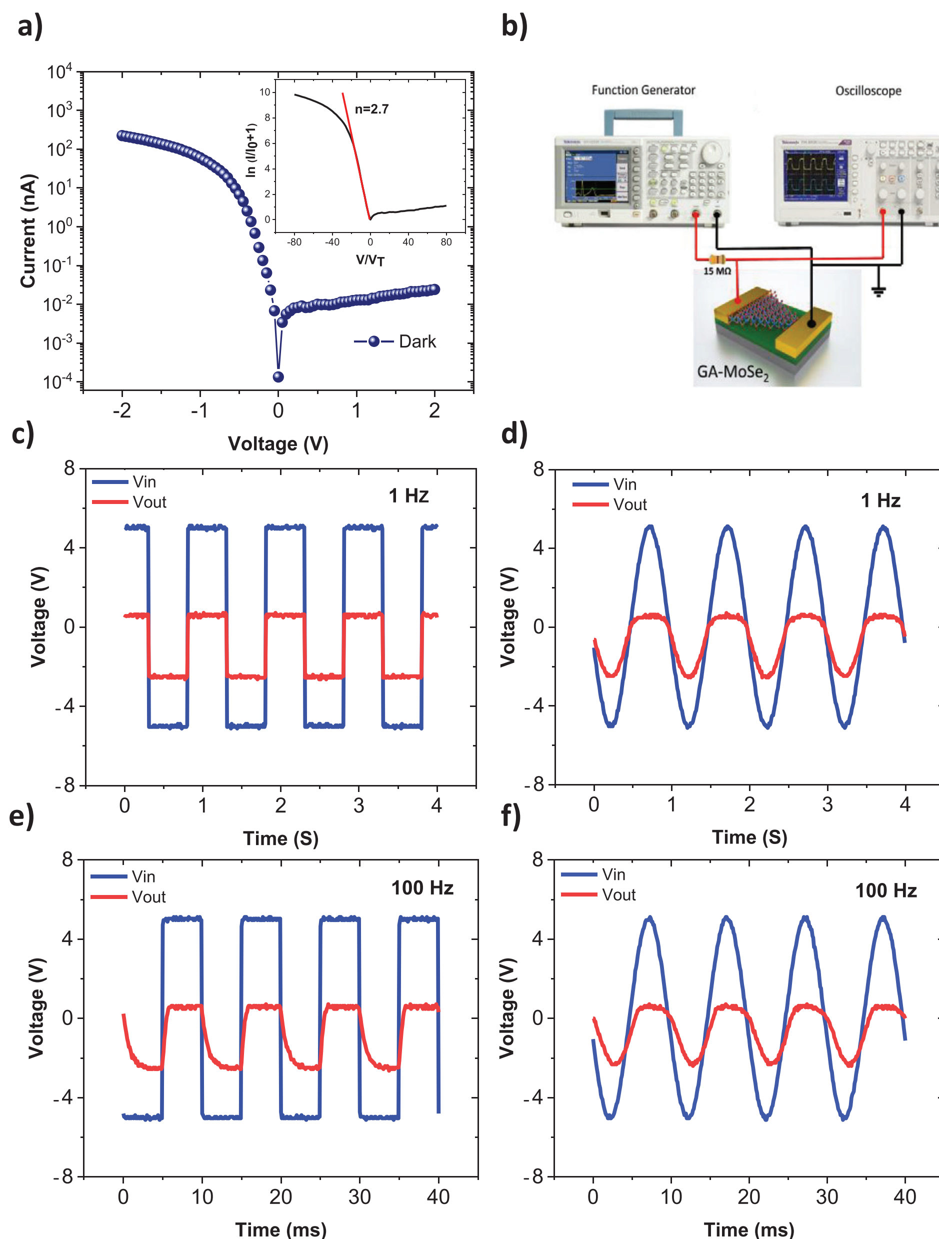

Figure 2. Dynamic rectifying behavior of the GA-$MoSe_2$ device. a) The log-scale *I–V* characteristics of the GA-$MoSe_2$ device under dark conditions. The inset shows the $\ln(\frac{I}{I_0}+1)$ versus $\frac{V}{V_T}$ curve with the ideality factor of n = 2.7. b) Schematic illustration of the rectifier measurement system for GA-$MoSe_2$ devices. c) square and d) sine waveform input and output voltage signal at 1 Hz. e) square and f) sine waveform input and output voltage signal at 100 Hz.

calculated to be n = ≈2.7 (inset of Figure 2a), which is comparable to many previously reported 2D materials-based diodes.[26–31] Note that the ideality factor (n) is derived from the inverse slope of the linear portion of the $\ln(\frac{I}{I_0}+1)$ versus $\frac{V}{V_T}$ curve in the small voltage range, where $V_T = \frac{kT}{q}$ (V_T = 25 mV at room temperature) and I_o is the saturation current, k is Boltzmann's constant, and q is the unit charge.[32] The high rectification ratio and good ideality factor suggest the GA-$MoSe_2$ diode can be used for waveform rectification. Figure 2b shows the circuit configuration of the GA-$MoSe_2$ Schottky diode and the measurement setup. An AC sine or square waveform voltage with various frequencies, generated by a function generator, was applied to the device through a 15 MΩ resistor, and both the input and output signals were displayed on a digital oscilloscope. Figure 2c,d depict the rectified output signal when subjecting the diode to input sine and square waveforms with V_{in} = ±5 V at 1 Hz. Figure 2e,f demonstrates the output signals of the device under 100 Hz input signals for square and since waveforms, respectively. Furthermore, the device was investigated for higher frequencies up to 500 Hz which is a relatively high operation frequency compared to other reported Schottky-based TMD materials.[33] Figure S5

© 2024 The Author(s). Advanced Optical Materials published by Wiley-VCH GmbH

21951071, 0, Downloaded from https://onlinelibrary.wiley.com/doi/10.1002/adom.202401682 by Simon Fraser University, Wiley Online Library on [20/09/2024]. See the Terms and Conditions (https://onlinelibrary.wiley.com/terms-and-conditions) on Wiley Online Library for rules of use; OA articles are governed by the applicable Creative Commons License

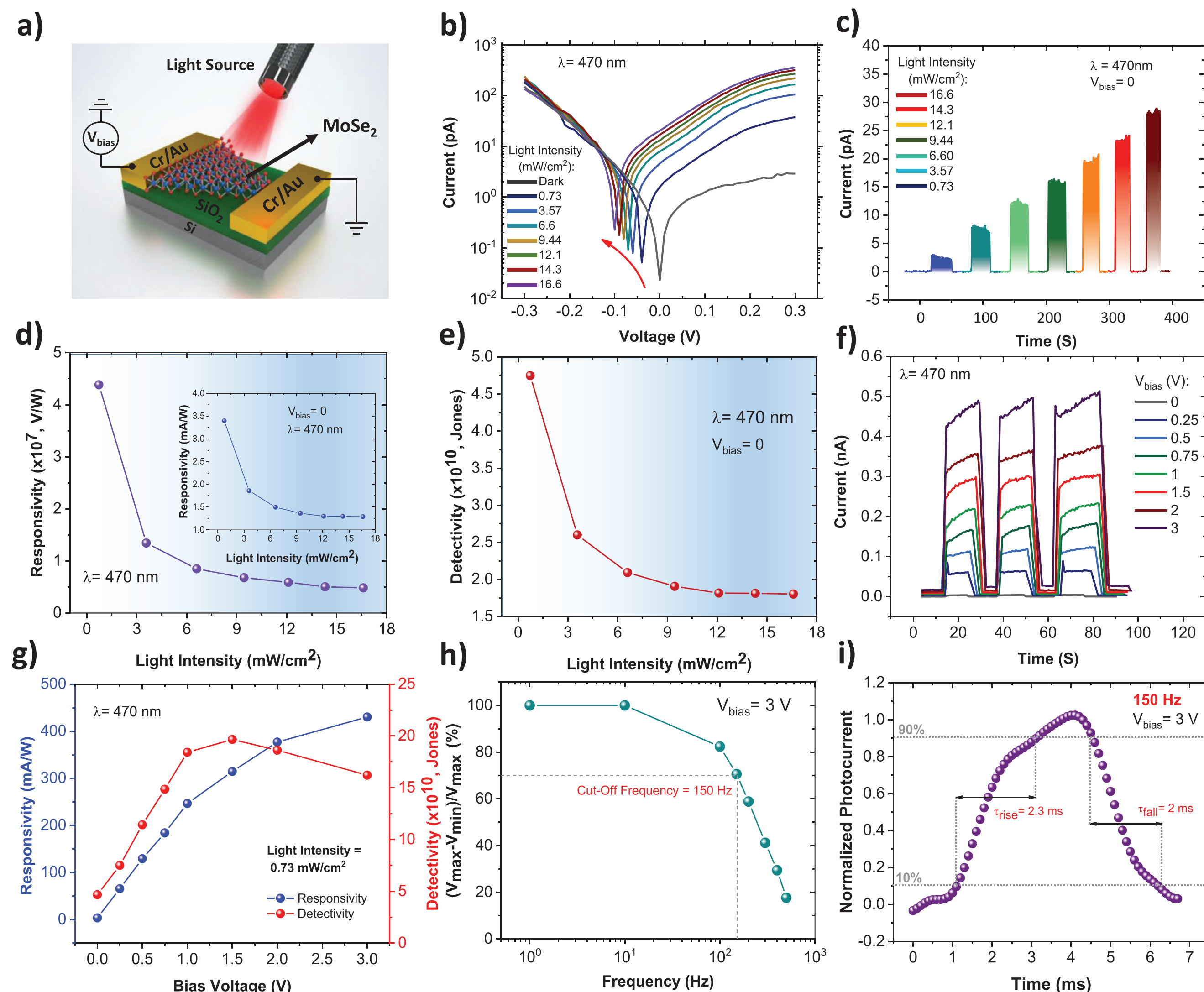

Figure 3. Photodetection characteristics of the GA-$MoSe_2$ device. a) Schematic illustration of a GA-$MoSe_2$ photodetector device. b) The *I*–*V* characteristics of the GA-$MoSe_2$ device under dark and light illumination (λ = 470 nm) at several light intensities from 0.73 to 16.6 mW cm^{-2} at zero bias voltage. c) The I–t characteristics of the GA-$MoSe_2$ device for the same range of intensities from 0.73 to 16.6 mW cm^{-2} at zero bias. d) The photovoltage responsivity (R_V) of the device at several light intensities at zero bias voltage. The inset shows the photocurrent responsivity of the device for the same range of intensities at zero bias. e) The photocurrent detectivity of the device at several light intensities at zero bias. f) The I–t characteristics of the GA-$MoSe_2$ device at several reverse bias voltages from 0.25 to 3 V under light intensity of 0.73 mW cm^{-2} (λ = 470 nm). g) The photocurrent responsivity (R_I) and detectivity (D^*) of the photodetector at several bias voltages with the same light intensity of 0.73 mW cm^{-2}. h) The normalized photoresponse as a function of incident light frequency (1–500 Hz) at a bias voltage of 3 V, shows a cut-off frequency of 150 Hz. i) The rise and fall times are 2.3 and 2 ms, respectively.

(Supporting Information) shows the device's half-wave rectifying performance at the frequencies of 10, 200, 300, and 500 Hz. At higher frequencies, the output signals have a small displacement compared to the input signals, which can be attributed to the parasitic capacitance induced by a large overlapping area between electrodes and substrate.[33]

The high diode rectification ratio of the GA-$MoSe_2$ device and the high optical absorption of $MoSe_2$ in the visible range[34] suggest the device can be used for photodetection. The schematic illustration of the device under illumination is shown in **Figure** 3a. The *I*–*V* characteristics of the device under dark conditions and light illumination (monochromatic LED, λ = 470 nm) with different intensities are illustrated in Figure 3b. The detection wavelength of 470 nm was used due to the strong light absorption of $MoSe_2$ at this wavelength.[35] By increasing the light intensity from 0.73 to 16.6 mW cm^{-2}, an increase in the open-circuit voltage (V_{oc}) from −40 to −100 mV was observed. The device also exhibited a low dark current of ≈23 fA at zero bias, which is significantly lower than many previously reported geometrically asymmetric photodetectors.[21,36–38] The low dark current in GA-$MoSe_2$ devices could be due to a few factors including the high crystalline quality of $MoSe_2$ with few defects[39] and relatively high Schottky barrier heights at the $MoSe_2$/Cr contacts.[40] The *I*–*V* characteristics of this device over a larger voltage range (±2 V) at dark and

© 2024 The Author(s). Advanced Optical Materials published by Wiley-VCH GmbH

21951071, 0, Downloaded from https://onlinelibrary.wiley.com/doi/10.1002/adom.202401682 by Simon Fraser University, Wiley Online Library on [20/09/2024]. See the Terms and Conditions (https://onlinelibrary.wiley.com/terms-and-conditions) on Wiley Online Library for rules of use; OA articles are governed by the applicable Creative Commons License

light conditions are also shown in Figure S6 (Supporting Information). Figure 3c exhibits the I-t characteristics of the device at different light intensities and zero bias, showing a linear increase in photocurrent from ≈3 to ≈28 pA with increasing light intensity. Figure S7 (Supporting Information) illustrates the photocurrent amplitudes as a function of light intensity. The photovoltage responsivity (R_V), photocurrent responsivity (R_I), and photocurrent detectivity (D^*) of the GA-$MoSe_2$ device were calculated using Equations (1–4).[41,42]

$$I_{ph} = I_l - I_d \tag{1}$$

$$R_V = \frac{V_{OC}}{P \times S} \tag{2}$$

$$R_I = \frac{I_{ph}}{P \times S} \tag{3}$$

$$D^* = \frac{S^{1/2} R}{\left(2eI_d\right)^{1/2}} \tag{4}$$

where I_{ph}, I_l, and I_d are the photocurrent, current under illumination, and dark current, respectively. P, S, and e are the light intensity, the effective surface area of the device, and the electron charge constant, respectively.

A high self-powered photovoltage responsivity of ≈4.38×10^7 V W^{-1} was obtained under photo-illumination with an intensity of 0.73 mW cm^{-2} (Figure 3d). The photovoltage responsivities range from ≈1.34×10^7 to ≈0.48×10^7 V W^{-1} for light intensities of 3.47–16.6 mW cm^{-2} at zero bias voltage (Figure 3d). The decline in photovoltage responsivity can be attributed to higher charge carrier recombination at higher light intensities.[27] Note that the area of the device under illumination used in our calculation is S = 125 μm^2 (Figure S8, Supporting Information). Table S1 (Supporting Information) presents a comparison between the self-powered photovoltage responsivity of our GA-$MoSe_2$ photodetector with previously reported 2D materials-based devices working in self-powered photovoltage mode. The inset of Figure 3d shows the self-powered photocurrent responsivity as a function of light intensity, showing a maximum value of ≈3.4 mA W^{-1} at 0.73 mW cm^{-2}. Figure 3e illustrates the bias-free photocurrent detectivity (D^*) of the device for a variety of light intensities with a maximum value of ≈4.75×10^{10} Jones at 0.73 mW cm^{-2}. Note that the photocurrent responsivity can significantly increase under non-zero voltage biases. Figure 3f depicts the I-t characteristics of the diode under several bias voltages (0–3 V) at a constant light intensity of 0.73 mW cm^{-2}. The photocurrent increases from ≈3 to ≈392 pA by increasing the bias voltage from 0 to 3 V, which could be due to the facilitation of photogenerated electrons/holes collection under non-zero bias voltages.[10] The photoresponsivity of the device reaches high values of ≈314 and ≈430 mA W^{-1} at 1.5 and 3 V bias voltages, respectively. The detectivity also increased to a maximum value of ≈1.96×10^{11} at 1.5 V (Figure 3g). The detectivity starts decreasing at the bias voltages above 1.5 V, which is due to the increase in dark current.[27] To evaluate the effect of incident light pulse frequency on the photodetection performance, a function generator connected to an LED was used to illuminate the GA-$MoSe_2$ device by light pulses with various frequencies, and the voltage across a 15 MΩ resistor connected to the device was recorded through an oscilloscope. The normalized photocurrent amplitude as a function of light pulse frequency is demonstrated in Figure 3h, showing a high cut-off frequency of ≈150 Hz. The frequency at which the photocurrent amplitude declines by a factor of 70% is known as the cut-off frequency.[43] Figure S9 (Supporting Information) shows the normalized I-t characteristics of the photodetector under light pulse illumination with different frequencies of 1, 10, 100, 150, 200, and 300 Hz, respectively, at 3 V bias voltage. The rise and fall times of the photocurrent were obtained to be ≈2.3 and ≈2 ms at the light frequency of 150 Hz and applied bias voltage of 3 V. The time required for the photoresponse to increase from 10% to 90% of its amplitude is known as the rise time, and the fall time is the time required to decline from 90% to 10%.[44] The GA-$MoSe_2$ photodetector also demonstrated excellent stability over 2000 on-off light cycles with a light frequency of 10 Hz (Figure S10, Supporting Information).

The gate voltage was not applied to the device in the measurements in Figure 3. The transfer characteristics of a geometrically symmetric device under dark conditions demonstrate that the $MoSe_2$ channel is p-type (Figure S11, Supporting Information). To further investigate the photodetection properties of such devices, the GA-$MoSe_2$ device was characterized under several applied gate biases (**Figure 4**). The schematic of the GA-$MoSe_2$ device with three inputs of incident light, gate voltage (V_{gs}), and drain-source voltage (V_{ds}) is shown in Figure 4a. Figure 4b illustrates the linear *I–V* characteristics of the device under gate biases of V_{gs} = −15, −10, −5, 0, 5, 10, and 15 V at dark conditions. When a negative V_{gs} is applied to the device, the concentration of the holes in the $MoSe_2$ channel increases, resulting in an increase in the level of current because the $MoSe_2$ channel is p-type. On the other hand, when a positive V_{gs} is applied to the device, the electron concentration surges, which leads to a less conductive channel and lower current. The I-t characteristics of the device under several gate voltages (i.e., −15–15 V) at a constant light intensity of 0.73 mW cm^{-2} and V_{ds} = 3 V are shown in Figure 4c. The photocurrent increases from ≈134 pA to ≈1.47 nA by changing the gate voltage from 15 to −15 V due to the gate modulation of the carrier concentrations in the p-type $MoSe_2$ channel and changes in the current rectification ratio (Figure 4c). The corresponding photocurrent responsivity and detectivity of the GA-$MoSe_2$ as a function of gate biases are demonstrated in Figure 4d, showing a maximum responsivity and detectivity of ≈1615 mA W^{-1} and ≈5.05×10^{11} at V_{gs} = −15 V, respectively. The photocurrent, responsivity, and detectivity of the GA-$MoSe_2$ under different gate biases with V_{ds} = 0 V are also shown in Figure S12 (Supporting Information), demonstrating a responsivity and detectivity of ≈11 mA W^{-1} and ≈1.5×10^{11} at V_{gs} = −15 V, respectively. Figure S13 (Supporting Information) shows the External Quantum Efficiency (EQE) values of the GA-$MoSe_2$ device at different light intensities and zero bias, showing the highest EQE for the lowest light intensity of 0.73 mW cm^{-2}. The light intensity-dependent EQE has previously been observed in geometrically asymmetric WSe_2 devices.[19] The EQE was also calculated with different applied voltage biases (V_{ds} = 0–3 V) and gate voltage biases (V_{gs} = −15–15 V), demonstrating the maximum EQE of ≈426.5% with a combination of V_{ds} = 3 V and V_{gs} = −15 V.

Table 1 presents a comparison between our GA-$MoSe_2$ photodetection performance with previously reported 2D $MoSe_2$-based photodetectors in terms of wavelength (λ), maximum

© 2024 The Author(s). Advanced Optical Materials published by Wiley-VCH GmbH

21951071, 0, Downloaded from https://onlinelibrary.wiley.com/doi/10.1002/adom.202401682 by Simon Fraser University, Wiley Online Library on [20/09/2024]. See the Terms and Conditions (https://onlinelibrary.wiley.com/terms-and-conditions) on Wiley Online Library for rules of use; OA articles are governed by the applicable Creative Commons License

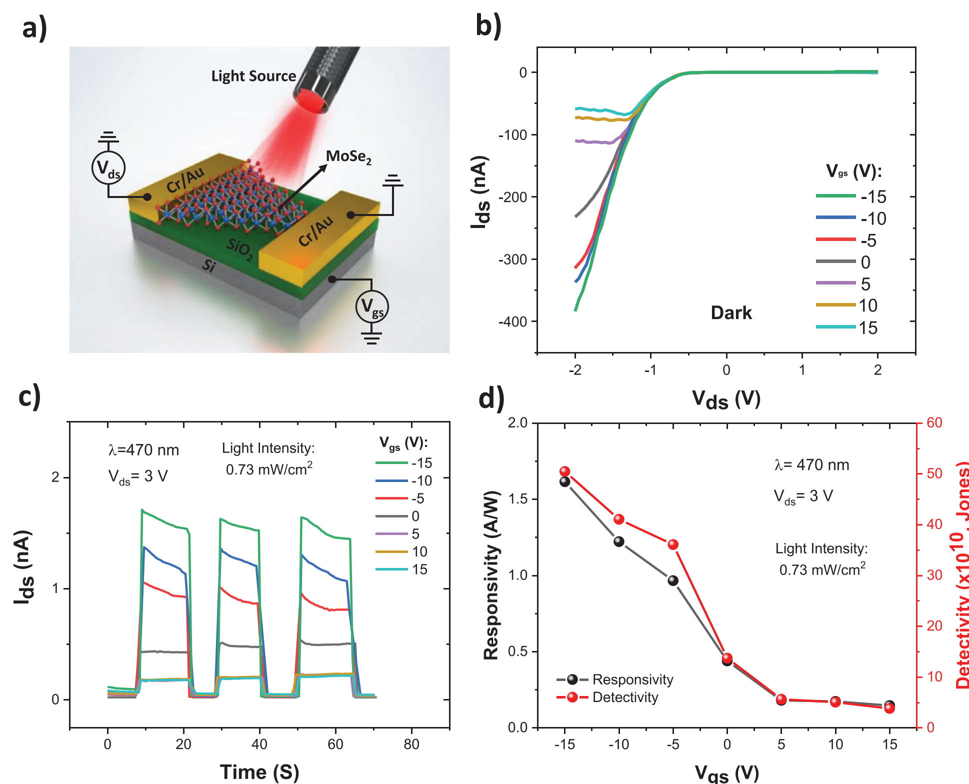

Figure 4. The effect of gate voltage on the photodetection performance of GA-$MoSe_2$ device. a) Schematic illustration of a GA-$MoSe_2$ photodetector device with drain-source voltage (V_{ds}) and gate-source voltage (V_{gs}). b) The *I–V* characteristics of the GA-$MoSe_2$ device at several gate biases of −15–15 V under dark conditions. c) The I–t characteristics of the GA-$MoSe_2$ device at the light intensity 0.73 mW cm^{-2}, V_{ds} = 3 V, and different gate biases of V_{gs} = −15–15 V. d) The photocurrent responsivity (R_I) and detectivity (D^*) of the photodetector as a function of gate voltage with the same light intensity of 0.73 mW cm^{-2}.

photocurrent responsivity (R_{max}), maximum photocurrent detectivity (D^*_{max}), bias voltage, and response time. The GA-$MoSe_2$ devices offer high photodetection performance and fast response time, in addition to a simple fabrication process as compared to the devices with vdWs stacking reported in Table 1 and Table S1 (Supporting Information). Traditional methods involve 2D materials transfer and layering multiple materials for vdWs heterostructures,[45,46] which results in material degradation or wrinkling.[47] On the other hand, a top-down approach can be used to scale up the fabrication of GA-$MoSe_2$ devices, utilizing large-scale growth of $MoSe_2$ via chemical vapor deposition (CVD)[48] or wet chemical processes,[49] followed by patterning and etching the $MoSe_2$ films into desired geometries for optimal optoelectronic performance.[23] It is also important to note

Table 1. Comparisons of the photodetection performance between the GA-$MoSe_2$ device and other 2D $MoSe_2$-based photodetection devices.

Device structure	λ [nm]	R_{max} [mA W^{-1}]	D^*_{max} [Jones]	Bias voltage	Response time	Ref.
Gr/$MoSe_2$/Si	650	270	7.13×10^{10}	V_{bias} = −5 V	270 ns	[51]
Gr/$MoSe_2$	650	89.5	2.24×10^{10}	V_{bias} = 0 V	9.6 ms	[52]
Monolayer $MoSe_2$	650	0.215	–	V_{bias} = 1 V	25 ms	[53]
$MoSe_2$	532	13	–	V_{bias} = 10 V	60 ms	[54]
$MoSe_2$	638	11.7	4.6×10^9	V_{bias} = 5 V	50 ms	[55]
Ta-doped $MoSe_2$	830	280	6.93×10^{10}	V_{bias} = 0 V	34 µs	[56]
$MoSe_2$/MoS_2	610	1300	2.6×10^{11}	V_{bias} = 5 V	0.6 s	[45]
$MoSe_2$/WSe_2	532	2000	–	V_{ds} = −2 V V_{gs} = −70 V	–	[46]
GA-$MoSe_2$	470	≈3.4	≈4.75×10^{10}	V_{bias} = 0 V	–	This Work
		≈314	≈1.96×10^{11}	V_{bias} = 1.5 V	–	
		≈430	≈1.62×10^{11}	V_{bias} = 3 V	≈2.3 ms	
		≈1615	≈5.05×10^{11}	V_{ds} = 3 V V_{gs} = −15 V	–	

© 2024 The Author(s). Advanced Optical Materials published by Wiley-VCH GmbH
21951071, 0, Downloaded from https://onlinelibrary.wiley.com/doi/10.1002/adom.202401682 by Simon Fraser University, Wiley Online Library on [20/09/2024]. See the Terms and Conditions (https://onlinelibrary.wiley.com/terms-and-conditions) on Wiley Online Library for rules of use; OA articles are governed by the applicable Creative Commons License

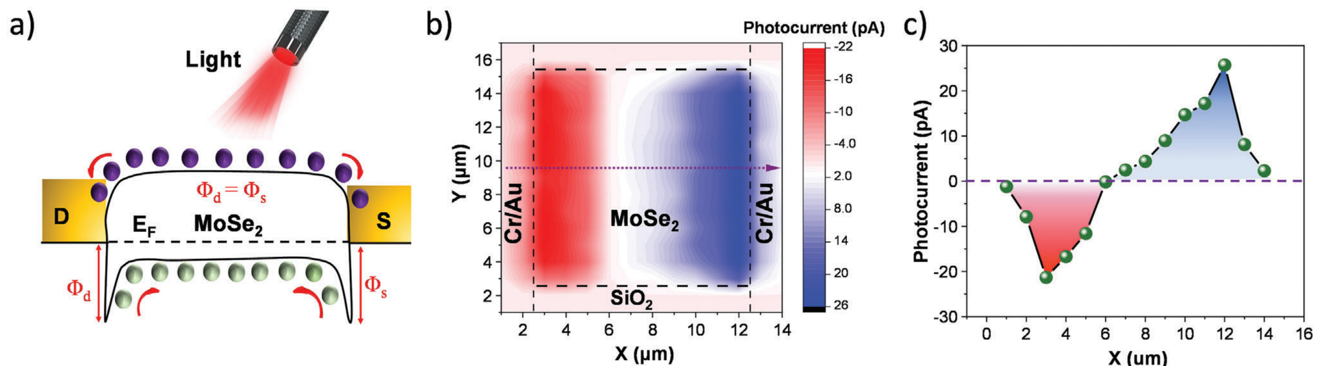

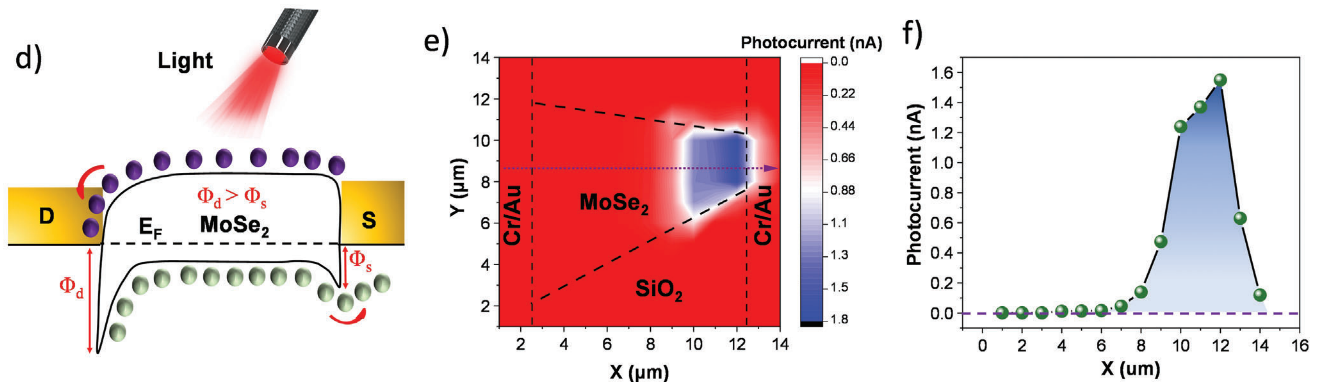

Figure 5. Working mechanism of the GA-$MoSe_2$ Schottky photodetector. a) Schematic illustration of energy band diagram for S-$MoSe_2$ devices with symmetric metal-$MoSe_2$-metal interfaces under light illumination. b) Photocurrent mapping of an S-$MoSe_2$ device using a 485 nm laser beam with a spot size of 1 μm^2. c) Photocurrent versus laser beam position along an S-$MoSe_2$ device at zero bias voltage, showing bidirectional photocurrents. d) Schematic illustration of energy band diagram for GA-$MoSe_2$ devices under light illumination. e) Photocurrent mapping of a GA-$MoSe_2$ device using a 485 nm laser beam with a spot size of 1 μm^2. f) Photocurrent versus laser beam position along a GA-$MoSe_2$ device at zero bias voltage, showing unidirectional photocurrents.

that the measured response time of the GA-$MoSe_2$ photodetector (≈2.3 ms) is limited by the measurement setup and the actual response could be much faster.[50]

To understand the physical mechanism of the photovoltaic effect and self-powered photodetection in such devices, energy band diagrams of the geometrically symmetric (S-$MoSe_2$) and asymmetric Cr-$MoSe_2$-Cr (GA-$MoSe_2$) devices were analyzed. **Figure 5a** shows the energy band diagram of an S-$MoSe_2$ device with equal Schottky barriers ($\Phi_1 = \Phi_2$) at the Cr-$MoSe_2$ interfaces. The non-rectifying behavior and negligible net photocurrent at zero bias in such devices (Figure S14, Supporting Information) are due to the Schottky barriers with equal heights at both sides. To understand the mechanism better, the 2D photocurrent mapping of the S-$MoSe_2$ device as a function of laser beam position at zero bias is performed (Figure 5b). A picosecond pulsed laser (λ = 485 nm) with a spot size of ≈1 µm and a motorized X-Y stage were used for this measurement. The photocurrent profile as a function of laser beam position along the dashed arrow in Figure 5b is shown in Figure 5c, indicating symmetrical charge collection with opposite polarities along the device,[57,58] which results in a photocurrent of about zero when the entire device is under illumination. The bidirectional photocurrents with opposite polarities observed in the S-$MoSe_2$ device can be attributed to the photogenerated carrier diffusion through the nearest Schottky barriers.[23,59] On the contrary, the Schottky barriers do not have equal heights in the GA-$MoSe_2$ device ($\Phi_1 > \Phi_2$, Figure S3, Supporting Information) due to the asymmetric Cr-$MoSe_2$ contact areas and asymmetrical distribution of surface states,[23] as shown in the band diagram schematic of the device (Figure 5d). The estimated Schottky barrier heights at the small and large $MoSe_2$/Cr contacts for both electrons and holes are presented in Section II, Supporting Information. Figure 5e,f illustrates the photocurrent mapping and profiling of the GA-$MoSe_2$, showing asymmetric photocurrent distribution with similar polarity along the device. The maximum photocurrent is observed when the laser beam is adjacent to the small Cr-$MoSe_2$ interface (X = ≈12 µm). Therefore, a non-zero photocurrent can be achieved when the entire device is under illumination at zero bias voltage (Figure S6, Supporting Information). The photocurrents at positions $1 < X < 7$ are nearly zero because photogenerated carriers are blocked

© 2024 The Author(s). Advanced Optical Materials published by Wiley-VCH GmbH

21951071, 0, Downloaded from https://onlinelibrary.wiley.com/doi/10.1002/adom.202401682 by Simon Fraser University, Wiley Online Library on [20/09/2024]. See the Terms and Conditions (https://onlinelibrary.wiley.com/terms-and-conditions) on Wiley Online Library for rules of use; OA articles are governed by the applicable Creative Commons License

by the large Schottky barrier at the large Cr-$MoSe_2$ interface and cannot reach the smaller interface due to the long travel distance and recombination[60] (Figure 5f).

The GA-$MoSe_2$ photodetectors can be used as wearable devices due to the excellent mechanical flexibility of $MoSe_2$ crystals.[61,62] The fabrication process of flexible GA-$MoSe_2$ devices is same as the SiO_2-supported devices (Figure S1, Supporting Information). Figure S15a (Supporting Information) shows a photograph image of the flexible GA-$MoSe_2$ Schottky device on a PET substrate. The inset shows the optical image of a GA-$MoSe_2$ device. To test the flexibility, a motorized linear stage was used to apply tensile strain to the devices. The self-powered photocurrents were recorded after a set of bending cycles (0, 50, 100, 500, and 1000 cycles). Figure S15b (Supporting Information) represents the normalized photocurrent of the flexible GA-$MoSe_2$ device as a function of bending cycles for two bending radii of R = 2 and R = 1 cm. The device showed excellent retention of 99% and 85% for the bending radii of R = 2 cm and R = 1 cm over 1000 bending cycles, respectively. The photoresponses after bending cycles are also shown in Figure S15c,d (Supporting Information). In this work, a proof-of-concept photodetector was fabricated using mechanically exfoliated $MoSe_2$ flakes. However, the 2D materials can be grown in wafer-scale sizes and etched in geometrically asymmetric shapes for the fabrication of an array of GA-$MoSe_2$ devices on a single chip. Hence, high photovoltaic performance, excellent flexibility, fast response time, and simple fabrication process make the GA-$MoSe_2$ photodetectors promising candidates for wearable optoelectronic applications.

3. Conclusion

The geometrically asymmetric photodetector devices based on Au-Cr-$MoSe_2$-Cr-Au structures have been demonstrated for the first time. A high current rectification ratio of $\approx 10^4$ and a large self-powered photovoltage responsivity of 4.38×10^7 V W^{-1} under 470 nm wavelength were achieved, making these devices suitable for electronic and optoelectronic applications. Furthermore, the GA-$MoSe_2$ device showed high photocurrent responsivity and detectivity of $\approx$430 mA W^{-1} and $\approx 1.62 \times 10^{11}$ Jones, respectively, along with a fast response time of $\approx$2.3 ms at 3 V bias. In addition, the gate modulation of carrier concentration in the $MoSe_2$ channel results in a high photocurrent responsivity of $\approx$1615 mA W^{-1} at a gate bias of −15 V. Therefore, the high rectification ratio, responsivity, detectivity, response time, and flexibility along with the simple fabrication process make the GA-$MoSe_2$ devices a promising candidate for high-performance electronic and optoelectronic applications.

4. Experimental Section

Fabrication of Geometrically Asymmetric $MoSe_2$ Devices: The fabrication process of the devices started with the exfoliation of $MoSe_2$ flakes from bulk $MoSe_2$ crystals (grown by chemical vapor transport (CVT) method, 2D Semiconductors) on a 300 nm SiO_2 deposited on Si substrates through mechanical exfoliation using a Nitto SPV224 tape. The SiO_2/Si substrate was cleaned through a three-step cleaning with acetone, IPA, and DI water in bath sonication before the exfoliation. Subsequently, two Cr/Au (10/60 nm) electrodes were deposited on both sides of the $MoSe_2$ after the lithography process in a way that the crystal has asymmetrical overlapping areas with the contact electrodes at both sides (Figure S1, Supporting Information). The photolithography was performed using a Microposit S1813 photoresist and MF-319 developer and metal deposition was carried out by thermal evaporation process with 0.2 and 0.5 Å s^{-1} deposition rate for chromium (Cr) and gold (Au), respectively.

Material Characterization: The thickness and morphology evaluation of the $MoSe_2$ flake was performed by an atomic force microscopy (AFM, Asylum MFP-3D) system. In addition, a Renishaw inVia confocal Raman microscope with a 514 nm continuous-wave excitation laser was used to record the Raman spectra of the GA-$MoSe_2$ sample. Moreover, to map the surface potential difference between $MoSe_2$ and Cr surfaces, a Kelvin probe force microscopy (KPFM, Bruker AFM System) was used.

Electrical/Optical Characterization: The GA-$MoSe_2$ devices were illuminated with monochromatic 470 nm LED light for the photodetection examinations, and the electrical measurements were conducted using a Keithley (SCS-4200) semiconductor measurement system within a probe station in an ambient environment. Function generator (Tektronix, AFG3151C) and oscilloscope (Tektronix, MDO3104) were used to examine the $MoSe_2$ diode characteristics as well as the optical frequency response and response time.

Supporting Information

Supporting Information is available from the Wiley Online Library or from the author.

Acknowledgements

This work was supported by the Natural Sciences and Engineering Research Council of Canada (NSERC), Canada Foundation for Innovation (CFI), British Columbia Knowledge Development Fund (BCKDF), Western Economic Diversification Canada (WD), and Simon Fraser University. The authors thank B. Kim for maintenance of the SFU Engineering Science cleanroom facility, Dr. D. Leznoff for access to Raman microscopy, and Mr. Ehsan Faridi for designing the figures schematics. The authors acknowledge CMC Microsystems and 4D LABS shared facilities that facilitated this research.

Conflict of Interest

The authors declare no conflict of interest.

Author Contributions

H.G. and A.A. contributed equally to this work. H.G. and A.A. performed all experimental design, fabrication, and measurements under the supervision of M.M.A. R.A., M.R.M., M.F., and A.H. participated in data analysis and scientific discussions. H.G. and A.A. wrote the manuscript. M.M.A. supervised the project and assisted with data analysis and manuscript preparation.

Data Availability Statement

The data that support the findings of this study are available from the corresponding author upon reasonable request

Keywords

2D diode, geometrically asymmetric architecture, $MoSe_2$ photodetector, $MoSe_2$, wearable electronics

Received: June 24, 2024
Revised: August 30, 2024
Published online:

© 2024 The Author(s). Advanced Optical Materials published by Wiley-VCH GmbH

21951071, 0, Downloaded from https://onlinelibrary.wiley.com/doi/10.1002/adom.202401682 by Simon Fraser University, Wiley Online Library on [20/09/2024]. See the Terms and Conditions (https://onlinelibrary.wiley.com/terms-and-conditions) on Wiley Online Library for rules of use; OA articles are governed by the applicable Creative Commons License

[1] H. Qiao, Z. Huang, X. Ren, S. Liu, Y. Zhang, X. Qi, H. Zhang, *Adv. Opt. Mater.* **2020**, *8*, 1900765.
[2] W. Tian, Y. Wang, L. Chen, L. Li, *Small* **2017**, *13*, 1701848.
[3] Y. Zhu, V. Raj, Z. Li, H. H. Tan, C. Jagadish, L. Fu, *Adv. Mater.* **2021**, *33*, 2105729.
[4] M. S. Tsai, T. L. Shen, H. M. Wu, Y. M. Liao, Y. K. Liao, W. Y. Lee, H. C. Kuo, Y. C. Lai, Y. F. Chen, *ACS Appl. Mater. Interfaces* **2020**, *12*, 9755.
[5] T. L. Shen, Y. W. Chu, Y. K. Liao, W. Y. Lee, H. C. Kuo, T. Y. Lin, Y. F. Chen, *Adv. Opt. Mater.* **2020**, *8*, 1901334.
[6] L. Peng, L. Hu, X. Fang, *Adv. Funct. Mater.* **2014**, *24*, 2591.
[7] X. Hu, X. Li, G. Li, T. Ji, F. Ai, J. Wu, E. Ha, J. Hu, *Adv. Funct. Mater.* **2021**, *31*, 2011284.
[8] J. Guo, G. Cheng, Z. Du, *Nanotechnology* **2020**, *31*, 292003.
[9] X. Han, M. Chen, C. Pan, Z. L. Wang, *J. Mater. Chem.* **2016**, *4*, 11341.
[10] A. Abnavi, R. Ahmadi, H. Ghanbari, M. Fawzy, M. R. Mohammadzadeh, F. Kabir, M. M. Adachi, *Adv. Opt. Mater.* **2024**, *12*, 2302651.
[11] R. Beiranvand, *Phys. E* **2021**, *126*, 114416.
[12] Y. Li, J. Shi, Y. Mi, X. Sui, H. Xu, X. Liu, *J. Mater. Chem. C* **2019**, *7*, 4304.
[13] J. Xia, J. Yan, Z. X. Shen, *FlatChem* **2017**, *4*, 1.
[14] A. Daus, S. Vaziri, V. Chen, Ç. Köroğlu, R. W. Grady, C. S. Bailey, H. R. Lee, K. Schauble, K. Brenner, E. Pop, *Nat. Electron.* **2021**, *4*, 495.
[15] L. Lv, J. Yu, M. Hu, S. Yin, F. Zhuge, Y. Ma, T. Zhai, *Nanoscale* **2021**, *13*, 6713.
[16] C. P. Veeramalai, S. Feng, X. Zhang, S. Pammi, V. Pecunia, C. Li, *Photonics Res.* **2021**, *9*, 968.
[17] J. Han, C. Fang, M. Yu, J. Cao, K. Huang, *Adv. Electron. Mater.* **2022**, *8*, 2100987.
[18] C. Zhou, S. Zhang, Z. Lv, Z. Ma, C. Yu, Z. Feng, M. Chan, *npj 2D Mater.Appl.* **2020**, *4*, 46.
[19] C. Zhou, S. Raju, B. Li, M. Chan, Y. Chai, C. Y. Yang, *Adv. Funct. Mater.* **2018**, *28*, 1802954.
[20] J. Lu, Z. Zheng, J. Yao, W. Gao, Y. Xiao, M. Zhang, J. Li, *Nanoscale* **2020**, *12*, 7196.
[21] W. Gao, S. Zhang, F. Zhang, P. Wen, L. Zhang, Y. Sun, H. Chen, Z. Zheng, M. Yang, D. Luo, *Adv. Electron. Mater.* **2021**, *7*, 2000964.
[22] J. Chen, Z. Zhang, J. Feng, X. Xie, A. Jian, Y. Li, H. Guo, Y. Zhu, Z. Li, J. Dong, *Adv. Mater. Interfaces* **2022**, *9*, 2200075.
[23] A. Abnavi, R. Ahmadi, H. Ghanbari, M. Fawzy, A. Hasani, T. De Silva, A. M. Askar, M. R. Mohammadzadeh, F. Kabir, M. Whitwick, *Adv. Funct. Mater.* **2023**, *33*, 2210619.
[24] D. Nam, J. U. Lee, H. Cheong, *Sci. Rep.* **2015**, *5*, 17113.
[25] A. Abnavi, R. Ahmadi, A. Hasani, M. Fawzy, M. R. Mohammadzadeh, T. De Silva, N. Yu, M. M. Adachi, *ACS Appl. Mater. Interfaces* **2021**, *13*, 45843.
[26] S. Kumar, A. Sanger, H. K. Chourasiya, A. Kumar, K. Asokan, R. Chandra, V. K. Malik, *J. Alloys Compd.* **2019**, *797*, 582.
[27] H. Ghanbari, A. Abnavi, A. Hasani, F. Kabir, R. Ahmadi, M. R. Mohammadzadeh, M. Fawzy, T. De Silva, M. M. Adachi, *Nanotechnology* **2023**, *34*, 285207.
[28] M. Moun, A. Singh, R. Singh, *Physica Status Solidi* **2018**, *215*, 1800188.
[29] F. Giannazzo, G. Fisichella, A. Piazza, S. Di Franco, I. Oliveri, S. Agnello, F. Roccaforte, *Mater. Sci. Semicond. Process.* **2016**, *42*, 174.
[30] J. K. Kim, K. Cho, T. Y. Kim, J. Pak, J. Jang, Y. Song, Y. Kim, B. Y. Choi, S. Chung, W. K. Hong, *Sci. Rep.* **2016**, *6*, 1.
[31] B. H. Moon, G. H. Han, H. Kim, H. Choi, J. J. Bae, J. Kim, Y. Jin, H. Y. Jeong, M. K. Joo, Y. H. Lee, *ACS Appl. Mater. Interfaces* **2017**, *9*, 11240.
[32] S. M. Faraz, W. Shah, N. U. H. Alvi, O. Nur, Q. U. Wahab, *Adv. Condens. Matter Phys.* **2020**, *2020*, 1.
[33] J. Y. Wu, Y. T. Chun, S. Li, T. Zhang, D. Chu, *ACS Appl. Mater. Interfaces* **2018**, *10*, 24613.
[34] J. Wu, Y. Liu, Y. Yao, Y. Shao, X. Wu, *J. Alloys Compd.* **2021**, *877*, 160317.
[35] L. Tao, Z. Chen, Z. Li, J. Wang, X. Xu, J. B. Xu, *InfoMat* **2021**, *3*, 36.
[36] H. Wang, H. Huang, J. Zha, Y. Xia, P. Yang, Y. Zeng, Y. Liu, R. Cao, B. Wang, W. Wang, *Adv. Opt. Mater.* **2023**, *11*, 2301508.
[37] G. Dushaq, M. Rasras, *ACS Appl. Mater. Interfaces* **2021**, *13*, 21499.
[38] X. Fu, T. Li, Q. Li, C. Hao, L. Zhang, D. Fu, J. Wang, H. Xu, Y. Gu, F. Zhong, *Mater. Horiz.* **2022**, *9*, 3095.
[39] S. Ghosh, G. Sun, T. A. Morgan, G. T. Forcherio, H. H. Cheng, G. E. Chang, *Sensors* **2023**, *23*, 7531.
[40] Z. Huang, Y. Mao, G. Lin, X. Yi, A. Chang, C. Li, S. Chen, W. Huang, J. Wang, *Opt. Express* **2018**, *26*, 5827.
[41] S. Ghosh, A. Varghese, K. Thakar, S. Dhara, S. Lodha, *Nat. Commun.* **2021**, *12*, 3336.
[42] S. Schuler, J. E. Muench, A. Ruocco, O. Balci, D. v. Thourhout, V. Sorianello, M. Romagnoli, K. Watanabe, T. Taniguchi, I. Goykhman, *Nat. Commun.* **2021**, *12*, 3733.
[43] D. Baierl, B. Fabel, P. Lugli, G. Scarpa, *Org. Electron.* **2011**, *12*, 1669.
[44] X. Hu, X. Zhang, L. Liang, J. Bao, S. Li, W. Yang, Y. Xie, *Adv. Funct. Mater.* **2014**, *24*, 7373.
[45] X. Chen, Y. Qiu, H. Yang, G. Liu, W. Zheng, W. Feng, W. Cao, W. Hu, P. Hu, *ACS Appl. Mater. Interfaces* **2017**, *9*, 1684.
[46] H. Xue, Y. Wang, Y. Dai, W. Kim, H. Jussila, M. Qi, J. Susoma, Z. Ren, Q. Dai, J. Zhao, *Adv. Funct. Mater.* **2018**, *28*, 1804388.
[47] D. L. Duong, S. J. Yun, Y. H. Lee, *ACS Nano* **2017**, *11*, 11803.
[48] A. S. George, Z. Mutlu, R. Ionescu, R. J. Wu, J. S. Jeong, H. H. Bay, Y. Chai, K. A. Mkhoyan, M. Ozkan, C. S. Ozkan, *Adv. Funct. Mater.* **2014**, *24*, 7461.
[49] R. Ahmadi, A. Abnavi, A. Hasani, H. Ghanbari, M. R. Mohammadzadeh, M. Fawzy, F. Kabir, M. M. Adachi, *Small* **2024**, *20*, 2304988.
[50] X. Luo, *Transistor-Based Ge/Soi Photodetector For Integrated Silicon Photonics*, University of California, Berkeley, CA, USA, **2011**.
[51] J. Mao, Y. Yu, L. Wang, X. Zhang, Y. Wang, Z. Shao, J. Jie, *Adv. Sci.* **2016**, *3*, 1600018.
[52] B. Liu, C. Zhao, X. Chen, L. Zhang, Y. Li, H. Yan, Y. Zhang, *Superlattices Microstruct.* **2019**, *130*, 87.
[53] Y. H. Chang, W. Zhang, Y. Zhu, Y. Han, J. Pu, J. K. Chang, W. T. Hsu, J. K. Huang, C. L. Hsu, M. H. Chiu, *ACS Nano* **2014**, *8*, 8582.
[54] J. Xia, X. Huang, L. Z. Liu, M. Wang, L. Wang, B. Huang, D. D. Zhu, J. J. Li, C. Z. Gu, X. M. Meng, *Nanoscale* **2014**, *6*, 8949.
[55] T. J. Dai, X. D. Fan, Y. X. Ren, S. Hou, Y. Y. Zhang, L. X. Qian, Y. R. Li, X. Z. Liu, *J. Mater. Sci.* **2018**, *53*, 8436.
[56] F. Zhong, J. Ye, T. He, L. Zhang, Z. Wang, Q. Li, B. Han, P. Wang, P. Wu, Y. Yu, *Small* **2021**, *17*, 2102855.
[57] S. Fathipour, M. Remskar, A. Varlec, A. Ajoy, R. Yan, S. Vishwanath, S. Rouvimov, W. Hwang, H. Xing, D. Jena, *Appl. Phys. Lett.* **2015**, *106*, 022114.
[58] C. C. Wu, D. Jariwala, V. K. Sangwan, T. J. Marks, M. C. Hersam, L. J. Lauhon, *J. Phys. Chem. Lett.* **2013**, *4*, 2508.
[59] L. Hao, Y. Liu, Z. Han, Z. Xu, J. Zhu, *J. Alloys Compd.* **2018**, *735*, 88.
[60] H. Chang, W. Xianjie, M. Peng, Z. Lingli, S. Bingqian, L. Weilong, L. Zhe, Z. Yu, S. Yu, T. Jinke, *Appl. Mater. Interface* **2017**, *9*, 18362.
[61] P. M. Pataniya, S. A. Bhakhar, M. Tannarana, C. Zankat, V. Patel, G. Solanki, K. Patel, P. K. Jha, D. J. Late, C. Sumesh, *J. Colloid Interface Sci.* **2021**, *584*, 495.
[62] D. Zhou, G. Feng, H. Khosla, S. T. Retterer, B. Li, *Adv. Funct. Mater.* **2022**, *32*, 2201612.

© 2024 The Author(s). Advanced Optical Materials published by Wiley-VCH GmbH

21951071, 0, Downloaded from https://onlinelibrary.wiley.com/doi/10.1002/adom.202401682 by Simon Fraser University, Wiley Online Library on [20/09/2024]. See the Terms and Conditions (https://onlinelibrary.wiley.com/terms-and-conditions) on Wiley Online Library for rules of use; OA articles are governed by the applicable Creative Commons License